Title

Nitric oxide synthase domain interfaces regulate electron transfer and calmodulin activation

Journal

Proceedings of the National Academy of Sciences of the United States of America, 110(38)

ISSN

0027-8424

Authors

Smith, Brian C
Underbakke, Eric S
Kulp, Daniel W
et al.

Publication Date

2013-09-17

DOI

10.1073/pnas.1313331110

Peer reviewed

Nitric oxide synthase domain interfaces regulate electron transfer and calmodulin activation

Brian C. Smith[a], Eric S. Underbakke[a], Daniel W. Kulp[b], William R. Schief[b], and Michael A. Marletta[a,1]

Departments of [a]Chemistry and [b]Immunology and Microbial Science, The Scripps Research Institute, La Jolla, CA 92037

Edited by Robert T. Sauer, Massachusetts Institute of Technology, Cambridge, MA, and approved August 7, 2013 (received for review July 14, 2013)

Nitric oxide (NO) produced by NO synthase (NOS) participates in diverse physiological processes such as vasodilation, neurotransmission, and the innate immune response. Mammalian NOS isoforms are homodimers composed of two domains connected by an intervening calmodulin-binding region. The N-terminal oxidase domain binds heme and tetrahydrobiopterin and the arginine substrate. The C-terminal reductase domain binds FAD and FMN and the cosubstrate NADPH. Although several high-resolution structures of individual NOS domains have been reported, a structure of a NOS holoenzyme has remained elusive. Determination of the higher-order domain architecture of NOS is essential to elucidate the molecular underpinnings of NO formation. In particular, the pathway of electron transfer from FMN to heme, and the mechanism through which calmodulin activates this electron transfer, are largely unknown. In this report, hydrogen–deuterium exchange mass spectrometry was used to map critical NOS interaction surfaces. Direct interactions between the heme domain, the FMN subdomain, and calmodulin were observed. These interaction surfaces were confirmed by kinetic studies of site-specific interface mutants. Integration of the hydrogen–deuterium exchange mass spectrometry results with computational docking resulted in models of the NOS heme and FMN subdomain bound to calmodulin. These models suggest a pathway for electron transfer from FMN to heme and a mechanism for calmodulin activation of this critical step.

iNOS | NO signaling | flavin | hemoprotein

Nitric oxide (NO) has several essential functions in mammalian physiology. NO produced by the neuronal and endothelial nitric oxide synthase isoforms (nNOS and eNOS, respectively) initiates diverse signaling processes including vasodilation, myocardial function, and neurotransmission (1). The eNOS and nNOS isoforms are constitutively expressed and their activity responds to intracellular calcium concentrations. The inducible NOS isoform (iNOS) is transcriptionally controlled and produces NO as a cytotoxin at sites of inflammation or infection. Aberrant NO signaling contributes to a variety of diseases including stroke, hypertension, and neurodegeneration (2).

Mammalian NOS isoforms are homodimeric and composed of two principal domains: the N-terminal oxidase domain and C-terminal reductase domain, which are connected by an intervening calmodulin (CaM) binding region (Fig. 1*A*). The N-terminal oxidase domain contains the heme and tetrahydrobiopterin cofactors and the binding site for the substrate arginine. The reductase domain is further divided into the FMN-binding subdomain and the FAD/NADPH-binding subdomains. This array of cofactors works in concert to catalyze the conversion of arginine to the intermediate *N*-hydroxyarginine and, ultimately, citrulline and NO. NADPH and oxygen are consumed in the process. During catalysis, electrons are shuttled from the reductase domain of one monomer to the heme domain of the opposite monomer in the homodimer (Fig. 1*B*) (1, 3). Electron transfer is initiated by two-electron reduction of FAD by NADPH. FMN then accepts an electron from FAD to FMN through the interaction of the FMN subdomain with the FAD subdomain. This FMN subdomain interaction state is known as the input state (Fig. 1*B*). The FMN subdomain then donates this electron to the heme domain. However, in the input state, FMN is buried within the rest of the reductase domain and inaccessible to the heme domain (2, 4). Therefore, for electron transfer from FMN to heme the FMN subdomain must undergo a largely uncharacterized conformational change (~70 Å) in which the FMN subdomain interacts with the heme domain (3, 5). This FMN subdomain conformation is known as the output state (Fig. 1*B*). Understanding the mechanism of electron transfer from FMN to heme is particularly important as this electron transfer step is rate limiting in NOS catalysis (3).

Calmodulin is required for NOS catalyzed NO formation. Calmodulin binding to the helix connecting the heme and reductase domains releases the FMN subdomain from the input state (3). However, the extent of calmodulin interaction with the heme domain remains unclear. Establishing whether or not calmodulin forms a direct interface with the heme domain is necessary to determine the mechanism through which calmodulin activates the rate-limiting electron transfer to the heme. Currently, NOS structural information is limited to truncations encompassing the iNOS heme domain (6, 7), the nNOS reductase domain (NAPDH, FAD, and FMN subdomains) (4, 8), or the iNOS FMN subdomain bound to calmodulin (9). The protein interfaces constituting the output state of the FMN subdomain remain unknown (Fig. 1*B*), and the precise role of calmodulin in NOS catalysis is poorly understood.

Previous studies have attempted to define interactions between the heme and reductase domains using computational docking (9–11). However, selecting the catalytically relevant structure from many alternative models is difficult without direct experimental evidence delineating the protein–protein interfaces between the heme domain, FMN subdomain, and calmodulin.

Significance

The biological role of nitric oxide (NO) in mammalian physiology is now well established as a signaling molecule in the cardiovascular and nervous systems and as a chemical component in the host response to infection. NO is synthesized by the enzyme NO synthase (NOS). The structure of the entire NOS enzyme has not been solved, but the structure of isolated domains has been reported. In this study, we use a mass spectrometry approach (hydrogen–deuterium exchange) to find interaction surfaces of the native protein. These results were then used to generate NOS models, which revealed interaction surfaces that mediate NOS activity. These interacting surfaces provide insight into the conformational changes and residues necessary for regulating NOS activity.

Author contributions: B.C.S., E.S.U., D.W.K., W.R.S., and M.A.M. designed research; B.C.S., E.S.U., and D.W.K. performed research; B.C.S., E.S.U., D.W.K., W.R.S., and M.A.M. analyzed data; and B.C.S., E.S.U., D.W.K., W.R.S., and M.A.M. wrote the paper.

The authors declare no conflict of interest.

This article is a PNAS Direct Submission.

[1]To whom correspondence should be addressed. E-mail: marletta@scripps.edu.

This article contains supporting information online at www.pnas.org/lookup/suppl/doi:10.1073/pnas.1313331110/-/DCSupplemental.

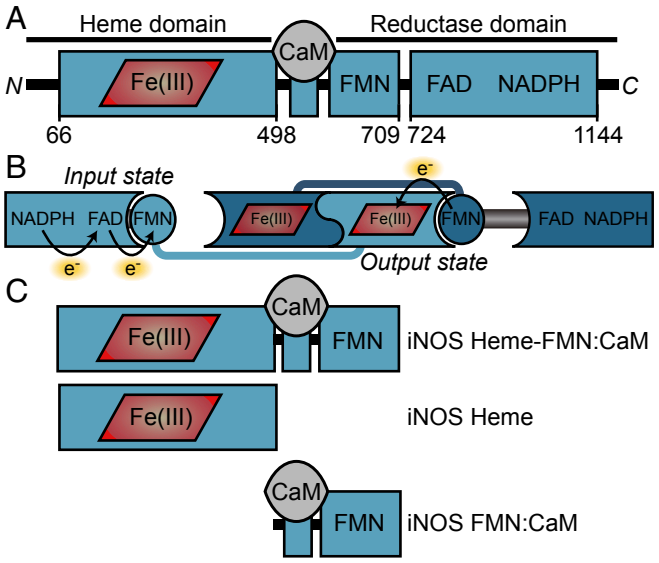

Fig. 1. Mammalian nitric oxidase synthases. (*A*) Mammalian nitric oxide synthase domain organization. (*B*) Nitric oxide synthase electron transfer pathway. In the input state, the FMN subdomain interacts with the FAD subdomain allowing electron transfer to occur between the flavin cofactors. In the output state, the FMN subdomain interacts with the heme domain allowing electron transfer between the FMN and heme. (*C*) iNOS constructs used in this study. iNOS heme-FMN:CaM consists of residues 66–709 bound to calmodulin. The hyphen in heme-FMN:CaM indicates the native covalent linkage of the heme domain and FMN subdomain and the colon indicates the noncovalent interaction of calmodulin with iNOS heme-FMN. iNOS heme consists of residues 66–498. iNOS FMN:CaM consists of residues 499–709 bound to calmodulin. All residue numbering refers to residues in murine iNOS.

We aimed to gain insight into the 3D domain organization of the NOS holoenzyme by probing interactions of isolated NOS domains using hydrogen–deuterium exchange mass spectrometry (HDX-MS). HDX-MS reports on the solvent accessibility and local environment of residues by measuring the exchange rate of backbone amide protons with the deuterons of a D_2O buffer (12, 13). Decreases in exchange rates are diagnostic of buried surfaces or decreased local backbone dynamics. Conversely, increased exchange rates reveal increased protein dynamics or loss of secondary structure. Monitoring exchange rate perturbations induced by a protein-binding partner can reveal interaction surfaces and conformational changes. Here, we mapped direct interactions between the heme domain, the FMN subdomain, and calmodulin using HDX-MS. Integration of the observed interaction surfaces and computational docking strategies generated models of the NOS output state that are consistent with kinetic analysis of iNOS and calmodulin mutants. These models suggest a well-defined pathway for electron transfer from FMN to heme and a mechanism for calmodulin activation of this critical electron transfer step.

Results

iNOS Constructs. To map nitric oxide synthase interaction surfaces, hydrogen–deuterium exchange rates were compared for three murine iNOS constructs: the isolated heme domain dimer (iNOS heme), the isolated FMN subdomain bound to calmodulin (iNOS FMN:CaM), and the contiguous heme domain and FMN subdomain bound to calmodulin (iNOS heme-FMN:CaM) (Fig. 1*C*). The termini of these constructs were chosen to match the constructs used for crystallization of the iNOS heme domain (6) and the iNOS FMN subdomain bound to calmodulin (9). Previous studies have shown that murine iNOS constructs lacking the FAD and NADPH binding subdomains (e.g., iNOS heme-FMN:CaM) have been used to study electron transfer between FMN and heme and therefore are excellent models of the FMN output state (14, 15).

Mapping Interactions of the iNOS Heme Domain. HDX-MS was used to compare the solvent accessibility of iNOS heme and iNOS heme-FMN:CaM (Fig. 1*C*). Slower exchange rates in iNOS heme-FMN:CaM were expected in regions of the heme domain that interact with the FMN subdomain or calmodulin. Full time courses for each unique peptide are shown in Fig. S1. Differences in percent exchange rate between iNOS heme and iNOS heme-FMN:CaM were mapped to the primary iNOS heme domain sequence (Fig. 2*A*). Several regions of the iNOS heme domain exhibited significant slowing of deuterium exchange when attached to the FMN:CaM module. No regions exhibited faster exchange in iNOS heme-FMN:CaM. Whereas decreases in dynamics may also contribute to the observed slower exchange rates, the HDX-MS data are consistent with the observed effects in the heme domain being primarily due to burial of protein–protein interaction interfaces. Mapping the regions displaying exchange rate perturbations to a crystal structure of the murine iNOS heme domain (6) revealed a clear interaction surface that spanned the iNOS heme domain dimer interface (Fig. 2*B*). Importantly, this interaction surface is of sufficient size to accommodate interactions with both the iNOS FMN subdomain and calmodulin.

Mapping Interactions of the iNOS FMN Subdomain with the Heme Domain. To elucidate the interaction surfaces between the FMN subdomain and the heme domain, HDX rates of iNOS FMN:CaM were compared with iNOS heme-FMN:CaM (Fig. 1*C*). Mapping the differences in exchange rate to the iNOS FMN subdomain primary sequence showed two regions with slowed exchange in iNOS heme-FMN:CaM (Fig. 3*A*). These regions correspond to the end of helix α19, helix α21, and the intervening loops surrounding FMN (Fig. 3*D*). In the 3D structure of the iNOS FMN subdomain, the two regions of primary sequence displaying slowed exchange map to one contiguous interaction surface surrounding FMN (Fig. 3*B*). The proximity of this interaction surface to FMN is consistent with this surface being important in directing electron transfer between FMN and heme. In addition, no regions displayed increased exchange rates in iNOS heme-FMN:CaM, suggesting that the observed differences are primarily due to burial of interaction surfaces between the FMN and heme domains.

Mapping Interactions of Calmodulin with the iNOS Heme Domain. To examine whether the iNOS heme domain contacts calmodulin when bound, the HDX rates of iNOS FMN:CaM and iNOS heme-FMN:CaM were compared (Fig. 1*C*). Three main regions displayed differences in exchange rate (Fig. 3*C*). Two regions—the AB loop and helices αF to αG—exhibited slower exchange rates in iNOS heme-FMN:CaM compared with iNOS FMN:CaM, indicative of burial in an interface with the iNOS heme domain. When mapped to the crystal structure of calmodulin bound to the iNOS FMN subdomain, these two regions overlapped into one contiguous interaction surface (Fig. 3*B*). A third region near the C terminus of calmodulin spanning helices G and H displayed a significant increase in exchange rate in iNOS heme-FMN:CaM (Fig. 3*D*). This increase in exchange rate is indicative of a conformational change or an increase in dynamics, resulting in increased solvent accessibility upon calmodulin binding to the heme domain.

Validation of iNOS HDX-MS Interfaces. To assess the functional relevance of the interfaces determined by HDX-MS, the results of previous mutagenesis studies were reevaluated in the context of the HDX-MS data. In regions not covered by previous

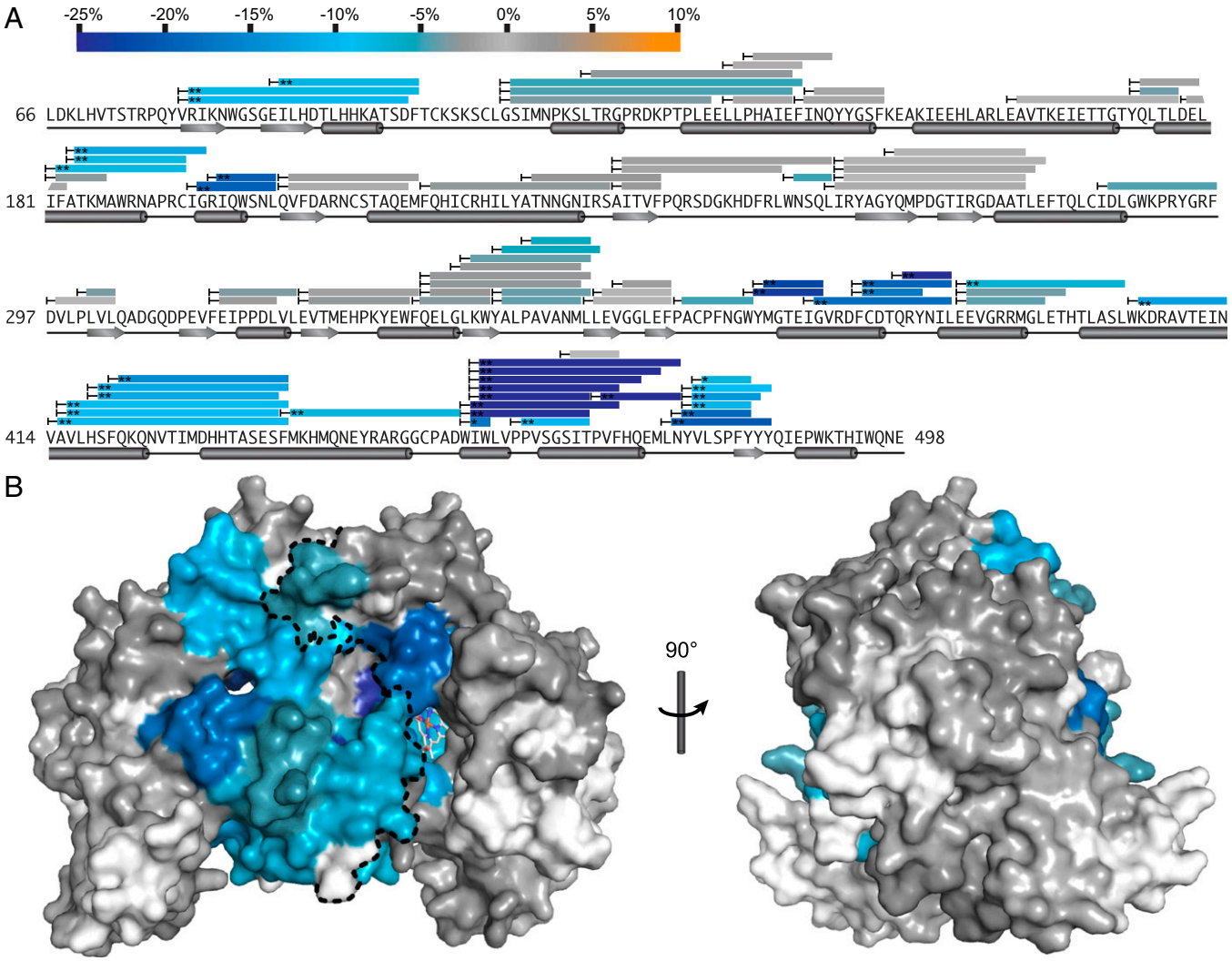

Fig. 2. HDX-MS results comparing exchange rates of iNOS heme-FMN:CaM to iNOS heme. (*A*) Bars above the iNOS primary sequence denote peptide coverage from HDX-MS analysis with secondary structure denoted below. Percent differences in exchange rates due to the native attachment of the FMN subdomain and calmodulin to the heme domain are color coded according to the scale bar. Differences were calculated as the average difference in percent deuterium incorporation over the actively exchanging portion of the time course. Peptides exhibiting slower exchange in iNOS heme-FMN:CaM are shown as a gradient of blue. Asterisks denote results of two-tailed, unpaired Student *t* tests at the time point exhibiting the maximum percent difference in exchange: $*P < 0.01$; $**P < 0.005$. (*B*) Color-coded HDX-MS results mapped to the surface of a murine iNOS heme domain crystal structure (PDB ID: 1DWV) (6). The HDX-MS dataset was consolidated for display over the 3D structure. For overlapping peptides that share start or end sites, the color of the shortest peptide was used. Otherwise the difference in percent deuterium incorporation was color coded based on the average for all overlapping peptide sequences. The dotted line (*Left*) indicates the heme domain dimer interface. Regions without HDX-MS peptide coverage are colored white.

mutagenesis data, residues within these regions were mutated to disrupt the interdomain interactions and subjected to kinetic analyses. The presteady-state rate of heme reduction and the steady-state rate of NADPH oxidation, cytochrome *c* reduction, 2,6-dichlorophenol-indophenol (DCIP) reduction, ferricyanide reduction, and NO formation were determined (Table S1). In all NOS isoforms and other P450 enzymes, cytochrome *c* is selectively reduced by FMN; DCIP is selectively reduced by either FAD or FMN; and ferricyanide is reduced by FAD, FMN, or heme (Fig. 4*D*) (3, 16). If a mutant perturbs either the interface between the FMN subdomain and the heme domain or the interface between calmodulin and the heme domain, then an increase in FMN solvent exposure is predicted. This increased exposure would lead to an increased rate of cytochrome *c* and, in some cases, DCIP reduction as well as a decreased rate of heme reduction and NO formation. Because the FAD, FMN, and heme cofactors can all reduce ferricyanide, ferricyanide reduction serves as a control to ensure that increases in cytochrome *c* reduction are due to increased FMN solvent exposure.

The interfaces determined by HDX-MS are entirely consistent with previous mutagenesis studies of rat nNOS and human iNOS (Fig. 4) (11, 16–21). Because our HDX-MS data were collected with murine iNOS, the corresponding residues in murine iNOS are discussed below. Previous mutagenesis studies showed that mutation of heme domain residues homologous to L226, N231, and R235 (Fig. 4*A*), and FMN subdomain residues homologous to D567 and Q568 (Fig. 4*B*), did not alter the rate of heme or cytochrome *c* reduction (11, 17). A separate mutagenesis study found that the residues homologous to F628, D654, and E655 did not alter NOS activity when FMN was bound (Fig. 4*B*) (16). A recent mutagenesis study demonstrated that mutation of Y99 in calmodulin to glutamate did not alter iNOS activity (Fig. 4*C*) (22). Based on the HDX-MS data, all of the aforementioned residues lie outside the interface between the FMN subdomain

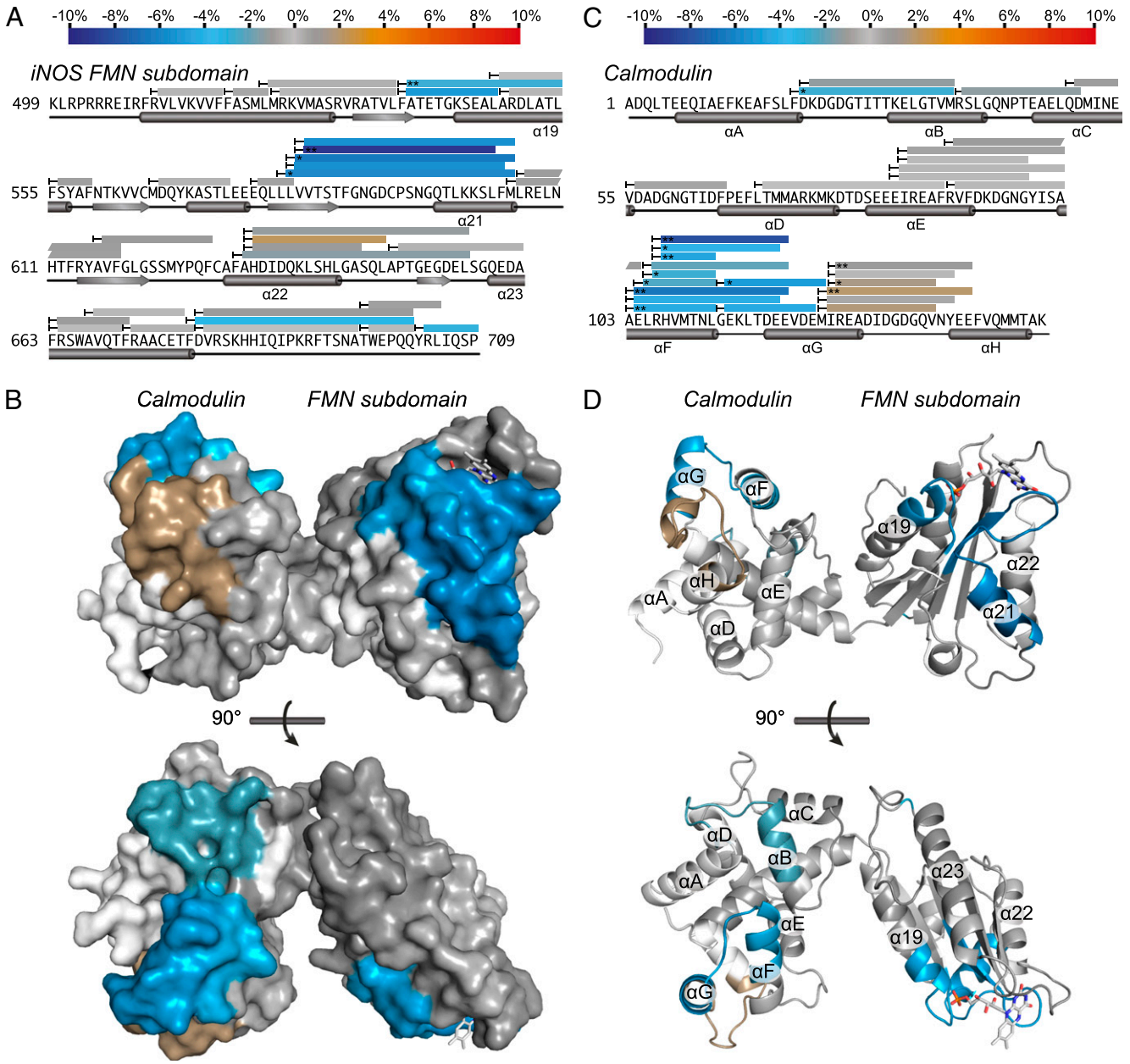

Fig. 3. HDX-MS results comparing exchange rates of iNOS heme-FMN:CaM to iNOS FMN:CaM. Percent differences in exchange rates due to the native linkage of the heme domain to the CaM-bound FMN subdomain are color coded according to the scale bar. Peptides exhibiting slower exchange in iNOS heme-FMN:CaM are shown as a gradient of blue. Peptides exhibiting faster exchange in iNOS heme-FMN:CaM are shown as a gradient of red. Asterisks denote results of two-tailed, unpaired Student *t* tests at the time point exhibiting the maximum percent difference in exchange: $*P < 0.05$; $**P < 0.01$. (*A*) Percent differences in HDX-MS exchange rate for the iNOS FMN subdomain. (*B*) Color-coded HDX-MS results mapped to a surface representation of a homology model of the murine iNOS FMN subdomain bound to calmodulin based on the crystal structure of the human iNOS FMN subdomain bound to calmodulin (PDB ID: 3HR4) (9). (*C*) Percent differences in HDX-MS exchange rate for calmodulin bound to iNOS. (*D*) Color-coded HDX-MS results mapped to a cartoon representation of the model of the murine iNOS FMN subdomain bound to calmodulin displayed in *B*. Helices are labeled as shown in *A* and *C*.

and the heme domain (Fig. 4). In contrast, several previous mutagenesis studies demonstrated that mutation of residues homologous to R189, W200, N202, T399, N424, K439, and R446 in the heme domain (Fig. 4*A*) and E540, D591, S594, and Q597 in the FMN subdomain (Fig. 4*B*) resulted in decreased rates of heme reduction and, in some cases, increased rates of cytochrome *c* reduction (11, 17–21). As predicted by the HDX-MS data, these rate changes are consistent with the roles of these residues in facilitating electron transfer from FMN to heme and forming the interfaces between the heme domain, the FMN subdomain, and calmodulin.

To complement the previous mutagenesis studies summarized above and validate the previously unknown iNOS interfaces determined by HDX-MS, charge reversal mutants at R80, E279, and E545 were generated. The R80E and E279R mutants were specifically designed to test the importance of the identified calmodulin docking site on the heme domain based on the computational modeling results (see below). E279 falls within a region that exhibited poor coverage in the HDX-MS results; yet, E279 was implicated in the interface with calmodulin. The E545R mutant was designed to further probe the FMN subdomain/heme domain interaction. Because the HDX-MS interface

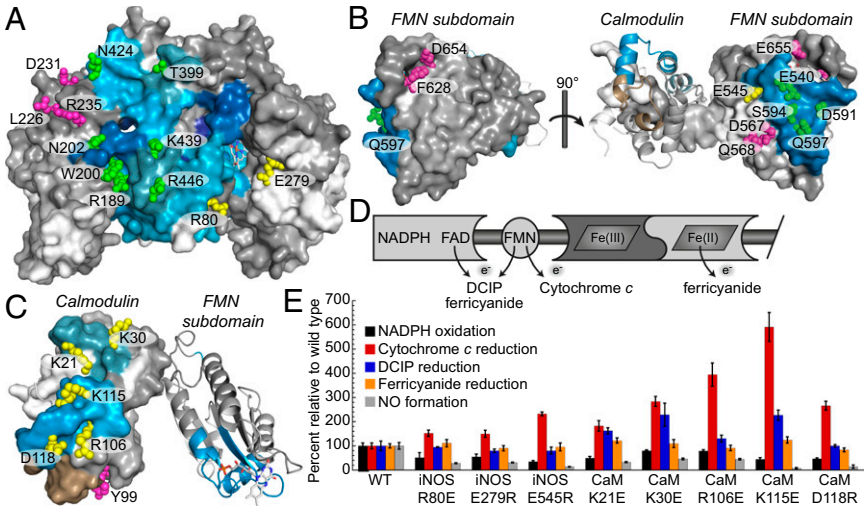

Fig. 4. Comparison of HDX-MS results with kinetic analysis of iNOS and calmodulin mutants. Previous mutagenesis studies have established residues that are predicted to lie within (green) or outside (magenta) the interfaces between the iNOS heme domain and the calmodulin-bound FMN subdomain. Residues mutated as part of the current study are colored yellow. Surfaces displaying altered deuterium exchange rates are color coded as in Figs. 2 and 3. (*A*) Residues mutated in the iNOS heme domain. (*B*) Residues mutated in the iNOS FMN subdomain. The FMN subdomain is shown in surface representation and calmodulin is shown in ribbon representation. (*C*) Residues mutated in calmodulin. Calmodulin is shown in surface representation and the FMN subdomain is shown in ribbon representation. (*D*) Summary of the cofactor specificity of the alternative electron acceptors used in this study. (*E*) Bar graphs of steady-state rates of NADPH oxidation (black), cytochrome *c* reduction (red), DCIP reduction (blue), ferricyanide reduction (orange), and NO formation (gray) for iNOS and calmodulin mutants. Rates were normalized to the rates for wild-type iNOS bound to calmodulin. Assays were performed as described in *Materials and Methods*. Error bars represent SD from the mean for at least three independent replicates.

residues of calmodulin were unexplored by point mutagenesis, charge reversal mutants of several residues (K21, K30, K115, R106, and D118) spanning the entire HDX-MS interface were analyzed (Fig. 4*C*). Importantly, none of these iNOS or calmodulin mutations significantly altered expression levels, cofactor binding (analyzed by absorbance spectroscopy), calmodulin binding (analyzed by SDS/PAGE), or dimer formation (analyzed by gel filtration chromatography). In addition, all mutants exhibited ferricyanide reduction rates within 25% that of wild type, indicating that none of the mutants significantly perturbed the overall rate of electron transfer through the reductase domain of iNOS. Therefore, the effects of the mutations could be restricted to interactions between the NOS subdomains or calmodulin. All mutations exhibited an increased rate of cytochrome *c* reduction and a decreased rate of NADPH oxidation, heme reduction, and NO formation. In addition, the calmodulin mutants exhibited greater increases in the rate of cytochrome *c* reduction than the iNOS mutants with the R106E (3.63 s^{-1}) and K115E (5.44 s^{-1}) mutants displaying the greatest increase compared with wild type (0.92 s^{-1}) among all tested mutants (Fig. 4*E* and Table S1). Taken together, these results indicate that direct binding of calmodulin to the heme domain is critical for efficient electron transfer from FMN to heme.

FMN fluorescence was used to probe the functional role of calmodulin in stabilizing the interface between the FMN subdomain and the heme domain. When the FMN subdomain is bound to the heme domain the heme cofactor quenches FMN fluorescence (5, 23, 24). Consequently, FMN fluorescence is a useful readout to monitor relative binding of the FMN subdomain to the heme domain. The CaM K115E mutant was used to disrupt the interface between the heme domain and calmodulin as it exhibited the greatest increase in cytochrome *c* reduction rate (5.44 s^{-1}) compared with wild type (0.92 s^{-1}) among all tested mutants (Fig. 4*E* and Table S1). The FMN fluorescence of iNOS heme-FMN:CaM WT was compared with iNOS heme-FMN:CaM K115E (Fig. S2). The maximum possible FMN fluorescence was measured in the construct missing the heme domain, iNOS FMN:CaM WT. As predicted, significant quenching of the FMN fluorescence was observed for iNOS heme-FMN:CaM WT (Fig. S2), indicating that the FMN subdomain is at least partially bound to the heme domain in iNOS heme-FMN:CaM WT. However, the FMN fluorescence of iNOS heme-FMN:CaM K115E was similar to that of iNOS FMN:CaM WT (Fig. S2), inferring that the calmodulin interface is necessary for the FMN subdomain to interact with the heme domain.

Computational Modeling of the iNOS Heme Domain and FMN Subdomain Bound to Calmodulin. Having validated the interaction surfaces determined by HDX-MS, this information was integrated with existing crystal structures to guide in silico modeling efforts and unveil plausible structural domain arrangements of the iNOS output state. First, to match the exact sequence used in the HDX-MS experiments the Rosetta molecular modeling platform (25) was used to generate homology models of the murine iNOS FMN subdomain bound to calmodulin based on the crystal structure of the human complex [Protein Data Bank (PDB) ID: 3HR4] (9). The human crystal structure contains four different conformations of calmodulin relative to the FMN subdomain (9), indicating that the linker between the calmodulin-binding helix and FMN subdomain is flexible. To account for this flexibility, the conformational space of the residues that connect the calmodulin-binding helix to the FMN subdomain was sampled during the modeling protocol (*Materials and Methods*). Crystal structures of the murine iNOS heme domain have already been determined (e.g., PDB ID: 3NW2) (7) so in this case no initial modeling was required.

To construct models of the iNOS output state, ensemble docking simulations (26) were used to dock a large set of calmodulin-bound FMN subdomain models onto the heme domain structure. The docking simulations produced 2,774 high-resolution models from 1,200 RosettaDock runs based on 100 different models for the calmodulin-bound FMN subdomain (*Materials and Methods*). Clustering analysis and filtering of models resulted in three closely related and plausible models of the iNOS output state (Fig. 5*A*, Table S2, and *Materials and Methods*). For simplicity, only one of the iNOS models is discussed below. To ensure that the iNOS models matched the HDX-MS data, the

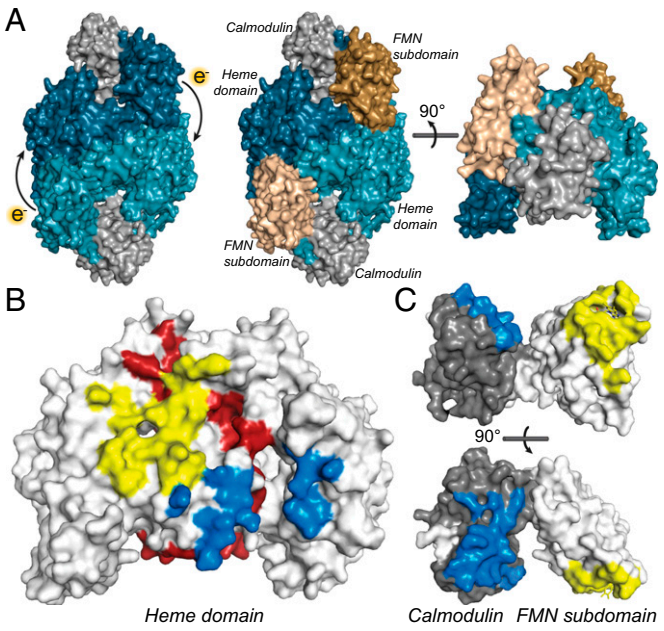

Fig. 5. Models of the iNOS heme domain complexed with the iNOS FMN subdomain and calmodulin. (*A*) Representative model (iNOS-3; Table S2) of the iNOS heme and FMN subdomains bound to calmodulin generated using Rosetta. (*Left*) iNOS monomers are colored blue and the calmodulins are colored gray. (*Center* and *Right*) FMN subdomains are highlighted in brown. (*B*) iNOS heme domain interaction surfaces with the FMN subdomain (yellow) and calmodulin (blue) as well as the heme domain dimer interface (red) on a surface representation of the iNOS heme domain (PDB ID: 1DWV) (6). (*C*) iNOS FMN subdomain (yellow) and calmodulin (blue) surfaces that interact with the iNOS heme domain in the Rosetta models. For *B* and *C*, residues were colored if they were present within the interface in at least two of the three iNOS Rosetta models or for calmodulin in the iNOS-3 model (Table S2) as analyzed using the KFC2 server (27).

interfaces determined by HDX-MS were then compared with the interfaces in the models determined using the Knowledge-based FADE and Contacts (KFC2) server (27). The observed HDX-MS interfaces of the heme domain result from: (*i*) interaction with the FMN subdomain, (*ii*) interaction with calmodulin, and (*iii*) stabilization of the heme domain dimer interface (Fig. 5*B*). The HDX-MS data correlated very well with the sum of these three interfaces present in the iNOS models. Similarly, the surfaces of calmodulin and the FMN subdomain that interact with the heme domain closely matched the interface determined by HDX-MS (Fig. 5*C*).

Kinetic Analysis of iNOS W366 Mutants. A particularly interesting feature of our iNOS models is the positioning of a conserved tryptophan (W366) nearly equidistant between the heme and FMN factors (Fig. 6*A* and Fig. S3). Because this residue was hypothesized to mediate long-range electron transfer from FMN to heme, W366 in full-length iNOS was mutated to alanine. The presteady-state rate of heme reduction along with the steady-state rate of NADPH oxidation, cytochrome *c* reduction, DCIP reduction, ferricyanide reduction, and NO formation was then determined for full-length iNOS W366A (Fig. 6*B* and Table S1). The rate of NO formation for the W366A mutant was below the detection limit of the assay ($\leq$0.03 s^{-1}) and the slowest of all mutants tested (Table S1). Unlike the other examined mutants, the W366A mutant displayed cytochrome *c*, DCIP, and ferricyanide reduction rates nearly identical to wild type (Fig. 6*B*). However, the rate of heme reduction was nearly three orders of magnitude slower for the W366A mutant compared with wild type (0.0047 s^{-1} vs. 3.79 s^{-1}), indicating a major heme reduction defect in the W366A mutant.

Discussion

Precise knowledge of the higher-order NOS domain architecture is necessary to fully understand the mechanisms controlling NO formation. Two critical pieces of the NOS mechanism—the pathway of electron transfer from FMN to heme and the mechanism through which calmodulin activates this electron transfer—have remained largely unknown, due to a lack of structural knowledge. Therefore, HDX-MS was used to map the critical interfaces between the heme domain, the FMN subdomain, and calmodulin. From these results, models of the iNOS output state bound to calmodulin were generated. To validate the HDX-MS interfaces used in generation of the iNOS output state models, the HDX-MS data were compared with the results of kinetic analyses of NOS mutants. Our mutagenesis results and previous studies identified several mutants that perturb electron transfer from the FMN subdomain to the heme domain (11, 17–21). Importantly, all of these residues are contained within the interfaces between the heme domain, FMN subdomain, and calmodulin identified by HDX-MS (Fig. 4). Likewise, several mutated residues exhibited little sensitivity to perturbation (11, 16, 17), consistent with their location outside the interfaces determined by HDX-MS (Fig. 4).

Calmodulin binding is generally thought to activate the synthesis of NO through two mechanisms (3). First, calmodulin binding destabilizes the input state, resulting in release of the FMN subdomain to interact with the heme domain or alternative

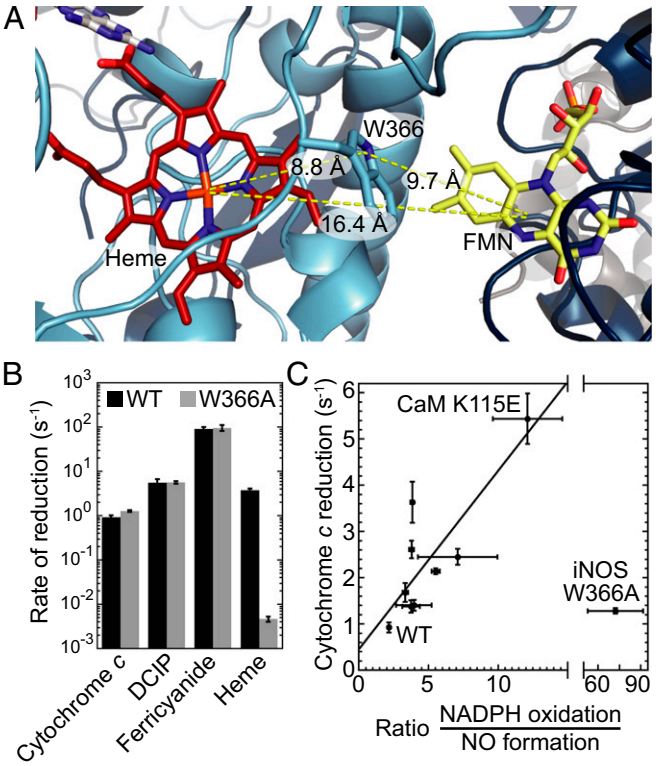

Fig. 6. iNOS W366 mediates electron transfer from FMN to heme. (*A*) iNOS output state highlighting W366, heme, and FMN in the iNOS-3 model (Table S2). (*B*) Comparison of rates of cytochrome *c*, DCIP, ferricyanide, and heme reduction for wild-type iNOS (black) and iNOS W366A (gray). (*C*) Plot of NOS uncoupling expressed as the ratio of NADPH oxidation to NO formation versus the rate of cytochrome *c* reduction. Rates were determined as described in *Materials and Methods*. Error bars represent SD from the mean for at least three independent replicates.

electron acceptors such as cytochrome *c*. Second, calmodulin stabilizes the interaction of the FMN subdomain with the heme domain to increase the rate of interdimer electron transfer from FMN to heme. Whereas calmodulin likely activates nNOS through both mechanisms (28–30), calmodulin binding to the isolated iNOS reductase domain does not increase the rate of cytochrome *c* reduction, suggesting that calmodulin activates iNOS solely by stabilizing the interaction of the FMN subdomain with the heme domain (28, 30, 31). Therefore, any effect of calmodulin mutation on iNOS catalysis can be localized to the output state.

Previous NOS computational modeling studies lacked the necessary experimental evidence to guide placement of calmodulin, and significant interaction between calmodulin and the heme domain had not been observed. Indeed, two studies omitted calmodulin entirely in their modeling (10, 23). Whereas two other NOS modeling studies included calmodulin, neither reported direct interaction of calmodulin with the heme domain (9, 11). To validate the interaction surface between calmodulin and the heme domain determined by HDX-MS, several residues that span this interface were subjected to charge-reversal mutagenesis and kinetic analyses (Fig. 4). These results affirm that an interface between calmodulin and the heme is formed during catalysis, and that this interface is necessary for efficient electron transfer from FMN to heme. Furthermore, the positioning of calmodulin on the heme domain in the iNOS output models is in agreement with a recent cryoelectron microscopy study that compared calmodulin-free and calmodulin-bound eNOS (32).

The observation of a direct interface between calmodulin and the heme domain presents clear mechanistic implications for calmodulin activation of NOS catalysis. Understanding factors that activate electron transfer from FMN to heme is particularly critical, as this step is rate limiting during catalysis (3). This slow rate of electron transfer from FMN to heme is due to the conformational change of the FMN subdomain required to shuttle electrons between the input and output states (3). This large conformational change is articulated at the hinges surrounding the calmodulin-binding helix (9, 33) (Fig. 7*A*). Indeed, generation of the models of the iNOS output state required a 40–80° rotation of the calmodulin-binding helix relative to the FMN subdomain compared with the conformations present in the crystal structure (PDB ID: 3HR4) (9) (Fig. S4). The interface between calmodulin and the heme domain in the calmodulin-docked state is essential to restrict movement of the FMN subdomain to conformations that align the FMN subdomain near the heme domain (Fig. 7*A*). Consistent with the importance of the calmodulin/heme domain interface, disruption of this interface resulted in greater increases in the rates of cytochrome *c* and DCIP reduction than did disruption of interface between the FMN subdomain and the heme domain (Fig. 4*E* and Table S1). Furthermore, disruption of calmodulin binding to the heme domain relieved quenching of FMN fluorescence by the heme domain (Fig. S2). Because increases in the rates of cytochrome *c*

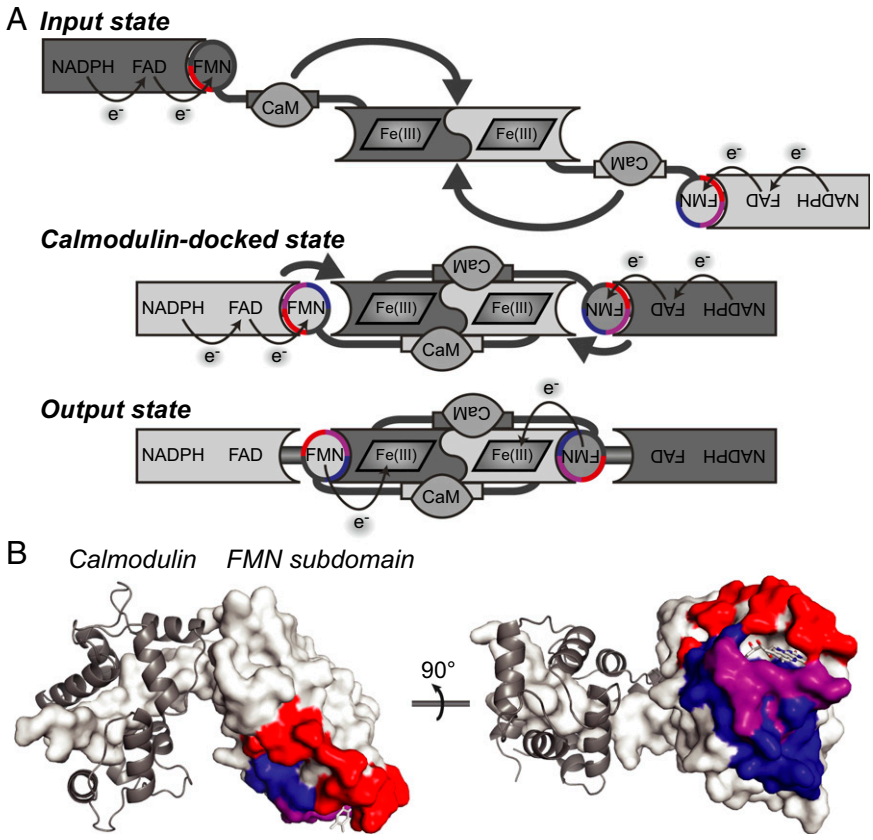

Fig. 7. Nitric oxide synthase electron transfer states. (*A*) Models of input state, calmodulin-docked state, and output state. The FMN subdomain is colored to match the distinct surfaces as shown in *B*. (*B*) The iNOS FMN subdomain uses distinct surfaces to interact with the FAD subdomain versus the heme domain. The surface of the FMN subdomain that interacts with the FAD domain (red) in the input state was determined from the structure of the rat nNOS reductase domain without calmodulin bound (PDB ID: 1TLL) (4) using the KFC2 server (27). The surface of the FMN subdomain that uniquely interacts with the heme domain in the electron output state was determined through HDX-MS analysis and is colored blue. The surface of the FMN subdomain that interacts with both the FAD subdomain and heme domain is colored magenta.

and DCIP reduction are indicative of increased FMN solvent exposure, these results suggest that the calmodulin-docked state (Fig. 7*A*) precedes the output state and the calmodulin-docked state is required for efficient alignment of the FMN and heme cofactors and subsequent electron transfer in the output state. Interestingly, calmodulin binds over the tunnel that allows the arginine substrate access to the heme active site (Fig. 5). This suggests that calmodulin binding may retain the intermediate *N*-hydroxyarginine in the heme active site until fully processed to NO and citrulline. After initial formation of the calmodulin-docked state from the input state, subsequent rounds of electron transfer likely cycle between the calmodulin-docked state and the output state (Fig. 7*A*).

The FMN subdomain must reduce both the heme as well as the tetrahydrobiopterin radical during catalysis. Because reduction of the tetrahydrobiopterin radical occurs through the heme (34), determining the interactions that position the FMN and heme at the optimal distance is especially critical. The iNOS output state models provide significant insights into the pathway of electron transfer from FMN to heme. Several previous studies place constraints on the distance between FMN and heme in the output state. One study found that FMN and heme are not magnetically linked in NOS, suggesting that the FMN and heme centers are separated by more than 15 Å (35). A subsequent pulsed EPR study determined that the distance between the N5 position of FMN and the heme iron is 18.8 Å (10). The distance of 16.4 Å measured in the iNOS models (Fig. 6*A*) also satisfies the distance constraints from a recent FMN fluorescence study (24). This distance precludes direct electron transfer between FMN and heme on the timescale necessary for NOS catalysis and suggests that NOS residues mediate electron transfer. Interestingly, W366 is positioned directly between the FMN and heme in the iNOS models (Fig. 6*A*). Similar positioning of homologous tryptophan residues has been observed in previous iNOS and nNOS computational docking studies (9, 11). As tryptophan residues often facilitate long-range electron transfer in proteins (36), W366 could serve as an intermediary to accelerate electron transfer between FMN and heme (9, 11, 37, 38). Furthermore, W366 is invariant among all eukaryotic NOS and the vast majority of bacterial NOS, suggesting a common heme reduction pathway through this tryptophan residue (Fig. S3). Interestingly, the only bacterial NOS that lack this tryptophan residue use an alternative N-terminal iron–sulfur cluster reductase domain in place of the typical C-terminal reductase domain (39).

Here, kinetic analyses indicated that all electron transfer processes up to transfer to FMN were unperturbed in the W366A mutant (Fig. 6*B*). However, a major decrease in the rate of heme reduction was observed for W366A, consistent with its predicted role in conducting electrons to the heme. Comparison of the cytochrome *c* reduction rate to the ratio of NADPH oxidation to NO formation further reinforced the role of W366 in facilitating electron transfer between the FMN and heme. An increase in the ratio of NADPH oxidation to NO formation reflects an increase in NOS uncoupling. For the vast majority of the mutants, an increase in NOS uncoupling correlated directly with an increase in the rate of cytochrome *c* reduction, indicating that uncoupling was due to disruption of FMN subdomain binding to the heme domain and increased FMN solvent exposure to alternative electron acceptors such as cytochrome *c* (Fig. 6*C*). The W366A mutant displayed the greatest uncoupling by far of any mutant tested while maintaining a rate of cytochrome *c* reduction near that of wild type. Taken together, the results indicate that the uncoupling the W366A mutant was not due to increased FMN solvent exposure, but instead due to very slow electron transfer from FMN to heme resulting from loss of this tryptophan residue.

The FMN subdomain shuttles electrons by interacting alternatively with heme domain and FAD subdomain (Fig. 1). Having mapped a docking interface and electron transfer pathway for the output state (i.e., FMN to heme), we next examined whether the same interface was responsible for input electron transfer (i.e., FAD to FMN). Therefore, the surface of the FMN subdomain that interacts with the rest of the reductase domain was determined using the KFC2 server (27) and a homology model of the iNOS reductase domain generated from the crystal structure of the rat nNOS reductase domain (PDB ID: 1TLL) (4). This surface was compared with the surface of the FMN subdomain that interacts with the heme domain as identified by HDX-MS (Fig. 7*B*). Interestingly, whereas there is significant overlap between these two interaction surfaces, the surface of the FMN subdomain that interacts with the FAD subdomain is distinct from the surface that interacts with the heme domain. This indicates that in future studies it may be possible to selectively perturb the interaction of the FMN subdomain with either the heme domain or FAD subdomain in the study of the input and output states.

In conclusion, integration of the HDX-MS results with computational docking and refinement allowed generation of models of the iNOS output state that are consistent with all available experimental data. The results presented here provide direct evidence that a functionally critical interaction between calmodulin and the heme domain is formed during heme reduction by the FMN subdomain. These models also suggest a clear pathway for electron transfer from FMN to heme through a conserved tryptophan residue, which was verified by mutation of this tryptophan and detailed kinetic analysis. Importantly, due to their conserved nature, these results are likely applicable to all three mammalian NOS isoforms.

Materials and Methods

Purification iNOS Heme-FMN:CaM. The iNOS heme-FMN expression vector was generated by cloning residues 66–709 of full-length murine iNOS with a forward primer encoding a N-terminal His_6 tag and NdeI restriction site (CGA ATT CCA TAT GCA CCA CCA CCA CCA CCT GGA CAA GCT GCA TGT G) and reverse primer encoding a HindIII restriction site (CCC AAG CTT ACG GGC TCT GGA TGA G) and ligated into the pCWori vector (40). The resulting iNOS heme-FMN expression vector was transformed into JM109 *Escherichia coli* along with a pACYC vector containing calmodulin (41). Overnight cultures were grown in Luria broth supplemented with 50 μg/mL ampicillin and 35 μg/mL chloramphenicol. Two 1-L expression cultures (Terrific broth, 50 μg/mL ampicillin, 35 μg/mL chloramphenicol) were inoculated with overnight culture (1:100 dilution) and grown to OD_{600} nm ~0.6–0.8 at 37 °C while shaking. Protein expression was induced with 1 mM isopropyl β-D-1-thiogalactopyranoside. Cultures were supplemented postinduction with final concentrations of 450 μM 5-aminolevulinic acid and 3 μM riboflavin to facilitate heme and FMN biosynthesis. The cultures were incubated overnight at 25 °C with shaking. Cell pellets were harvested by centrifugation and frozen at −80 °C.

Frozen cell pellets were thawed in buffer A (50 mM Hepes pH 7.5, 2 mM $CaCl_2$, 1 mM L-arginine, 250 mM NaCl, 1 mM β-mercaptoethanol, and 5% vol/vol glycerol) supplemented with 20 mM imidazole, 1 mM Pefabloc SC (Pentapharm), 1 μg/mL pepstatin, 1 μg/mL antipain, 10 μg/mL benzamadine, and 5 μg/mL DNase I. Cells were lysed by passage through an Emulsiflex-C5 high-pressure homogenizer at 20,000 psi (Avestin), and cell debris was removed by centrifugation at 135,000 × *g* for 30 min. The supernatant was applied to a column containing 3 mL Ni-NTA Superflow resin (Qiagen) pre-equilibrated with buffer A at 4 °C. The column was washed with 100 mL buffer A containing 20 mM imidazole. iNOS heme-FMN:CaM was eluted with 10 mL buffer A containing 150 mM imidazole. The eluted iNOS heme-FMN:CaM was then concentrated to ~3 mL using a 50,000 molecular weight cutoff Sartorius Vivaspin concentrator and further purified on a HiLoad Superdex 200 26/60 gel filtration column (GE Healthcare) using an isocratic flow of 50 mM Hepes pH 7.5, 50 mM NaCl, 1 mM DTT, 1 mM $CaCl_2$, 8 μM tetrahydrobiopterin, and 5% vol/vol glycerol. Fractions containing iNOS heme-FMN:CaM were pooled and concentrated to >250 μM. Aliquots were frozen in liquid N_2 and stored at −80 °C. Protein concentrations were determined using the Bradford method with BSA as the standard.

Purification of iNOS FMN:CaM. Residues 499–709 of murine iNOS were cloned, expressed, and purified as described above for iNOS heme-FMN:CaM with the following modifications: The forward primer used for PCR amplification (CGA ATT CCA TAT GCA CCA CCA CCA CCA CGA GAA GCT GAG GCC CAG G) encoded a NdeI restriction site and a His_6 tag followed by iNOS residue 499; aminolevulinic acid was not added during expression; arginine was not added to buffer A and lower concentrations of imidazole (5 mM) and NaCl (50 mM) were used; and tetrahydrobiopterin was not added to the gel filtration buffer.

Purification of iNOS Heme. The iNOS heme construct containing residues 66–498 of murine iNOS was expressed and purified as described above for iNOS heme-FMN:CaM with the following modifications: Riboflavin was not added during expression and $CaCl_2$ was not added to any of the buffers.

Mutagenesis, Expression, and Purification of Full-Length iNOS with Bound Calmodulin. Site-directed mutagenesis of full-length murine iNOS in the pCWori vector and calmodulin in the pACYC vector was performed using the QuikChange method (Stratagene) according to the manufacturer's protocol with the following exceptions: Annealing temperature for iNOS mutagenesis was lowered to 50 °C and extension time extended to 21 min. Expression and purification of wild-type or mutant full-length murine iNOS coexpressed with wild-type or mutant calmodulin was conducted as described previously (42, 43). Protein purity was assessed by SDS/PAGE and concentrations were determined using the Bradford method with BSA as the standard.

H/D Exchange Time Courses. Exchange time courses were performed as previously described (13) with minor modifications. Briefly, time courses were performed in triplicate with the following time points: 15, 30, 60, 120, 300, 900, 1,800, and 3,600 s. Three independent time courses were performed for each protein construct. To initiate exchange, protein stocks were diluted to 20 μM into D_2O buffered with 50 mM Hepes pD 7.5 (pD = $-\log[D_3O^+]$). Aliquots (50 μL) were withdrawn at various time points, quenched to pH ∼2.5 by addition of 2.5% vol/vol TFA, and frozen in liquid nitrogen. Rapidly thawed samples were digested (5 min, pH 2.3, 4 °C) with 200 μL 50% (vol/vol) immobilized pepsin (Pierce) that was prewashed in 0.025% TFA pH 2.5. Pepsin was removed by brief centrifugation, and digested sample was immediately frozen in liquid nitrogen and stored at −80 °C until MS analysis. Pepsin digests of hydrogen-deuterium exchange time courses were analyzed using an Agilent 1100 LC connected in-line with a Waters LCT Premier XE mass spectrometer (13). Agilent ZORBAX 300SB-C18 column (3.5 μm; 2.1 × 50 mm) and tubing were maintained at 4 °C during analysis. Unique pepsin digest peptides for LC-MS analysis were identified using an orthogonal acceleration quadrupole time-of-flight mass spectrometer connected in-line with an ultraperformance liquid chromatograph as previously described (13). HDX-MS data were analyzed using the HX Express macro (44) for Microsoft Excel. Deuteron incorporation was calculated as previously described (13) and plotted versus time. Percent deuterium exchange (%D) was calculated according to Eq. **1**, where d = deuterons incorporated, n = the number of amino acids in the peptide, p = the number of proline residues, and C is a correction factor accounting for the D_2O content of exchange reactions and back exchange (17%). Back exchange was estimated from the maximum exchange observed for peptides derived from iNOS heme-FMN:CaM that was incubated overnight in D_2O.

$$\%\mathrm{D} = d/(n - p - 1) \times 100 \times C \quad [1]$$

Exchange rate differences were determined by averaging Δ%D through the actively exchanging region of the time course as previously described (13).

iNOS Steady-State Activity Assays. All assays were performed in 300 μL total volumes in clear 96-well microplates. NO formation was monitored at 401 nm using the oxyhemoglobin (HbO_2) assay as previously described (45). Reactions contained 100 mM Hepes pH 7.5, 100 mM NaCl, 5 mM L-arginine, 200 μM NADPH, 8 μM HbO_2, and 30 nM full-length iNOS with bound calmodulin. NADPH oxidation was measured using the decrease in absorbance at 340 nm and an extinction coefficient of 6.22 $mM^{-1}{\cdot}cm^{-1}$. Reactions contained 100 mM Hepes pH 7.5, 100 mM NaCl, 5 mM L-arginine, 200 μM NADPH, and 30 nM iNOS/calmodulin. Cytochrome *c* reduction was measured at 550 nm (16) and an extinction coefficient of 21 $mM^{-1}{\cdot}cm^{-1}$. Reactions contained 100 mM Hepes pH 7.5, 100 mM NaCl, 200 μM NADPH, 65 μM cytochrome *c*, and 10 nM iNOS/calmodulin. DCIP reduction was measured at 600 nm (16) using an extinction coefficient of 20.6 $mM^{-1}{\cdot}cm^{-1}$. Reactions contained 100 mM Hepes pH 7.5, 100 mM NaCl, 200 μM NADPH, 100 μM DCIP, and 10 nM iNOS/calmodulin. Ferricyanide reduction was measured at 420 nm (16) using an extinction coefficient of 1.2 $mM^{-1}{\cdot}cm^{-1}$. Reactions contained 100 mM Hepes pH 7.5, 100 mM NaCl, 200 μM NADPH, 1 mM ferricyanide, and 10 nM iNOS/calmodulin.

Stopped-Flow Rate of Heme Reduction. Heme reduction by electron transfer from the reductase domain was followed by the formation of the ferrous–CO complex with a Soret maximum at 442 nm. Rates were determined at 25 °C using a HiTech KinetAsyst stopped-flow instrument equipped with a diode array detector. Before sample delivery into the stopped-flow syringes, the syringes were deoxygenated with an anaerobic dithionite solution. Residual dithionite was removed by rinsing the stopped-flow syringes with anaerobic buffer via three-way joints. The headspace of a Reacti-Vial (Pierce) containing 5 μM iNOS with bound calmodulin, 100 mM Hepes pH 7.5, 100 mM NaCl, and 5 mM L-Arg was exchanged with CO (99.99%; Praxair). A saturated CO solution containing 100 mM Hepes pH 7.5, 100 mM NaCl, and 100 μM NADPH was prepared by bubbling CO into the solution in a Reacti-Vial for >5 min. These two solutions were transferred to the stopped-flow syringes using anaerobic techniques and mixed to initiate heme reduction. UV-visible spectra were recorded from 300 to 700 nm for 2.25 s for iNOS WT to 450 s for iNOS W366A using the Kinetic Studio program (TgK Scientific). The increase in Soret maximum at 442 nm was fitted to a single or double exponential equation using Kaleidagraph (Synergy).

Determination of FMN Fluorescence. Fluorescence emission spectra were measured on a Horiba Jobin Yvon FluoroMax-4 spectrofluorimeter at 22 °C. Fluorescence was measured at a protein concentration of 1 μM in buffer (100 mM Hepes pH 7.5, 1 mM DTT) that was filtered (0.22 μm) and degassed with argon. Excitation and emission slits were set to 5 nm. Samples were measured in a quartz cuvette with a 1-cm path length. An excitation wavelength of 450 nm was used, and fluorescence emission was measured from 470 to 650 nm. Fluorescence emission spectra were smoothed using the Savitzky–Golay method. FMN fluorescence in iNOS constructs was measured at a concentration of 1 μM. Spectra were measured every ∼2 min until the signal stabilized generally within 5–10 min following dilution. To ensure differences in FMN fluorescence were not due to differences in FMN/heme occupancy or protein concentration, protein concentration and cofactor occupancy was normalized by the FMN and heme absorbance for iNOS heme-FMN:CaM and iNOS heme-FMN:CaM K115E and the FMN absorbance for iNOS FMN:CaM.

Structural Modeling. Computational protein modeling was used to produce low energy models for the iNOS output state that are consistent with experimental data. A series of 100 murine homology models based on the crystal structure of the human iNOS FMN subdomain bound to calmodulin (PDB ID: 3HR4) (9) were generated using the Rosetta molecular modeling platform (25). The conformational space of the six residues (534–539) that connect the calmodulin-binding helix to the FMN subdomain was sampled by a Rosetta loop modeling protocol (46). The 100 lowest energy conformations were selected and maintained as input models for the docking simulations. A structure of the murine iNOS heme domain (PDB ID: 3NW2) (7) was relaxed in Rosetta and also used as input for the docking simulations. The RosettaDock protocol (47) is composed of three main steps: initial perturbation, low-resolution searching, and high-resolution refinement. RosettaDock performs a global search over the whole protein surface using Monte Carlo sampling because enumerating all possible docking poses is computationally prohibitive. RosettaDock simulations were run with the following three constraints, all of which used a smoothed, square-well potential with a target distance range. First, the end of the heme domain (residue 487) and beginning of the FMN domain (residue 511) were constrained with a target distance of 15–50 Å to accommodate the intervening linker sequence. Second, in the output state, FMN and heme were constrained with a target distance of 10–20 Å because they must be close enough to allow electron transfer. Third, based on the HDX-MS data, calmodulin was hypothesized to directly interact with the heme domain, so calmodulin residues 21 and 115 were enforced to be close to one of the two heme monomers using a series of loose constraints. iNOS models produced by docking were filtered for their consistency with the HDX-MS data by evaluating the degree of burial (in the models) for interface residues identified by HDX-MS. Residues exhibiting significant decreases in HDX-MS exchange rates in iNOS heme-FMN:CaM were predicted to undergo at least partial burial upon binding in the structural model. The molecular software library structural bioinformatics platform was used to measure the change in solvent exposure upon complex formation in the models for the following residues: heme domains 80–102, 187–203, 366–386, 396–465, 471–485; FMN subdomains 538–547, 582–605; and calmodulin 20–36, 105–124 (48). The amount of surface area buried in the complex was computed for each residue by subtracting the solvent accessible surface area (SASA) in the isolated heme domain and isolated calmodulin-bound FMN subdomain from the

SASA in the modeled complex. The models with partial burial surface area were selected for further analysis; specifically a 33% buried SASA quantile was used as a cutoff. The resulting 88 models clustered into 18 groups using a complete-linkage hierarchical algorithm (49) with a 5-Å cutoff. The 18 clusters were further pruned to identify models that buried the maximal surface area of the HDX-MS patches; three clusters were identified using cutoffs of >290 Å^2 for the heme domain patch, >230 Å^2 for the FMN subdomain patch, >60 Å^2 for the calmodulin patch, and a distance between the C_α positions of K491 and R510 of <36 Å. To produce complete models of the iNOS heme domain and FMN subdomain bound to calmodulin in the output state, the missing linker between the FMN subdomain and heme domain was built for a representative model of each cluster using RosettaRemodel (46).

ACKNOWLEDGMENTS. We thank members of the M.A.M. laboratory for their comments and critical reading of the manuscript. LC-MS/MS instrumentation was acquired with National Institutes of Health (NIH) support (Grant 1S10RR022393-01). Financial support was provided by The Scripps Research Institute and NIH National Institute of General Medical Sciences Postdoctoral Fellowships 5F32GM095023 (to B.C.S.) and 5F32GM093564 (to E.S.U.). This is Manuscript 24070 from The Scripps Research Institute.

1. Förstermann U, Sessa WC (2012) Nitric oxide synthases: Regulation and function. *Eur Heart J* 33(7):829–837, 837a–837d.
2. Serafim RA, Primi MC, Trossini GH, Ferreira EI (2012) Nitric oxide: State of the art in drug design. *Curr Med Chem* 19(3):386–405.
3. Iyanagi T, Xia C, Kim J-JP (2012) NADPH-cytochrome P450 oxidoreductase: Prototypic member of the diflavin reductase family. *Arch Biochem Biophys* 528(1):72–89.
4. Garcin ED, et al. (2004) Structural basis for isozyme-specific regulation of electron transfer in nitric-oxide synthase. *J Biol Chem* 279(36):37918–37927.
5. Li W, Fan W, Elmore BO, Feng C (2011) Effect of solution viscosity on intraprotein electron transfer between the FMN and heme domains in inducible nitric oxide synthase. *FEBS Lett* 585(16):2622–2626.
6. Crane BR, et al. (2000) Structures of the N(omega)-hydroxy-L-arginine complex of inducible nitric oxide synthase oxygenase dimer with active and inactive pterins. *Biochemistry* 39(16):4608–4621.
7. Grädler U, et al. (2011) Novel nanomolar imidazo[4,5-b]pyridines as selective nitric oxide synthase (iNOS) inhibitors: SAR and structural insights. *Bioorg Med Chem Lett* 21(14):4228–4232.
8. Zhang J, et al. (2001) Crystal structure of the FAD/NADPH-binding domain of rat neuronal nitric-oxide synthase. Comparisons with NADPH-cytochrome P450 oxidoreductase. *J Biol Chem* 276(40):37506–37513.
9. Xia C, Misra I, Iyanagi T, Kim J-JP (2009) Regulation of interdomain interactions by calmodulin in inducible nitric-oxide synthase. *J Biol Chem* 284(44):30708–30717.
10. Astashkin AV, Elmore BO, Fan W, Guillemette JG, Feng C (2010) Pulsed EPR determination of the distance between heme iron and FMN centers in a human inducible nitric oxide synthase. *J Am Chem Soc* 132(34):12059–12067.
11. Tejero J, Hannibal L, Mustovich A, Stuehr DJ (2010) Surface charges and regulation of FMN to heme electron transfer in nitric-oxide synthase. *J Biol Chem* 285(35): 27232–27240.
12. Marcsisin SR, Engen JR (2010) Hydrogen exchange mass spectrometry: What is it and what can it tell us? *Anal Bioanal Chem* 397(3):967–972.
13. Underbakke ES, Iavarone AT, Marletta MA (2013) Higher-order interactions bridge the nitric oxide receptor and catalytic domains of soluble guanylate cyclase. *Proc Natl Acad Sci USA* 110(17):6777–6782.
14. Feng C, et al. (2006) Direct measurement by laser flash photolysis of intramolecular electron transfer in a two-domain construct of murine inducible nitric oxide synthase. *J Am Chem Soc* 128(11):3808–3811.
15. Ghosh DK, et al. (2006) Nitric-oxide synthase output state. Design and properties of nitric-oxide synthase oxygenase/FMN domain constructs. *J Biol Chem* 281(20): 14173–14183.
16. Adak S, Ghosh S, Abu-Soud HM, Stuehr DJ (1999) Role of reductase domain cluster 1 acidic residues in neuronal nitric-oxide synthase. Characterization of the FMN-FREE enzyme. *J Biol Chem* 274(32):22313–22320.
17. Panda K, et al. (2006) Surface charge interactions of the FMN module govern catalysis by nitric-oxide synthase. *J Biol Chem* 281(48):36819–36827.
18. Shimanuki T, Sato H, Daff S, Sagami I, Shimizu T (1999) Crucial role of Lys(423) in the electron transfer of neuronal nitric-oxide synthase. *J Biol Chem* 274(38):26956–26961.
19. Yadav J, Fujiwara S, Sagami I, Shimizu T (2004) Arg410 near the heme proximal ligand of neuronal nitric oxide synthase is critical for both substrate recognition and electron transfer. *Chem Lett* 33:752–753.
20. Yumoto T, Sagami I, Daff S, Shimizu T (2000) Roles of the heme proximal side residues tryptophan409 and tryptophan421 of neuronal nitric oxide synthase in the electron transfer reaction. *J Inorg Biochem* 82(1–4):163–170.
21. Haque MM, et al. (2009) Neutralizing a surface charge on the FMN subdomain increases the activity of neuronal nitric-oxide synthase by enhancing the oxygen reactivity of the enzyme heme-nitric oxide complex. *J Biol Chem* 284(29): 19237–19247.
22. Piazza M, Futrega K, Spratt DE, Dieckmann T, Guillemette JG (2012) Structure and dynamics of calmodulin (CaM) bound to nitric oxide synthase peptides: Effects of a phosphomimetic CaM mutation. *Biochemistry* 51(17):3651–3661.
23. Ilagan RP, et al. (2009) Regulation of FMN subdomain interactions and function in neuronal nitric oxide synthase. *Biochemistry* 48(18):3864–3876.
24. Ghosh DK, Ray K, Rogers AJ, Nahm NJ, Salerno JC (2012) FMN fluorescence in inducible NOS constructs reveals a series of conformational states involved in the reductase catalytic cycle. *FEBS J* 279(7):1306–1317.
25. Leaver-Fay A, et al. (2011) ROSETTA3: An object-oriented software suite for the simulation and design of macromolecules. *Methods Enzymol* 487:545–574.
26. Chaudhury S, Gray JJ (2008) Conformer selection and induced fit in flexible backbone protein-protein docking using computational and NMR ensembles. *J Mol Biol* 381(4): 1068–1087.
27. Zhu X, Mitchell JC (2011) KFC2: A knowledge-based hot spot prediction method based on interface solvation, atomic density, and plasticity features. *Proteins* 79(9): 2671–2683.
28. Newton DC, Montgomery HJ, Guillemette JG (1998) The reductase domain of the human inducible nitric oxide synthase is fully active in the absence of bound calmodulin. *Arch Biochem Biophys* 359(2):249–257.
29. Gachhui R, et al. (1996) Characterization of the reductase domain of rat neuronal nitric oxide synthase generated in the methylotrophic yeast Pichia pastoris. Calmodulin response is complete within the reductase domain itself. *J Biol Chem* 271 (34):20594–20602.
30. Montgomery HJ, Romanov V, Guillemette JG (2000) Removal of a putative inhibitory element reduces the calcium-dependent calmodulin activation of neuronal nitric-oxide synthase. *J Biol Chem* 275(7):5052–5058.
31. Rafferty S, Malech HL (1996) High reductase activity of recombinant NOS2 flavoprotein domain lacking the calmodulin binding regulatory sequence. *Biochem Biophys Res Commun* 220(3):1002–1007.
32. Persechini A, Tran Q-K, Black DJ, Gogol EP (2013) Calmodulin-induced structural changes in endothelial nitric oxide synthase. *FEBS Lett* 587(3):297–301.
33. Tejero J, Haque MM, Durra D, Stuehr DJ (2010) A bridging interaction allows calmodulin to activate NO synthase through a bi-modal mechanism. *J Biol Chem* 285 (34):25941–25949.
34. Wei C-C, et al. (2008) Catalytic reduction of a tetrahydrobiopterin radical within nitric-oxide synthase. *J Biol Chem* 283(17):11734–11742.
35. Perry JM, Moon N, Zhao Y, Dunham WR, Marletta MA (1998) The high-potential flavin and heme of nitric oxide synthase are not magnetically linked: Implications for electron transfer. *Chem Biol* 5(7):355–364.
36. Gray HB, Winkler JR (2010) Electron flow through metalloproteins. *Biochim Biophys Acta* 1797(9):1563–1572.
37. Crane BR, et al. (1997) The structure of nitric oxide synthase oxygenase domain and inhibitor complexes. *Science* 278(5337):425–431.
38. Crane BR, et al. (1998) Structure of nitric oxide synthase oxygenase dimer with pterin and substrate. *Science* 279(5359):2121–2126.
39. Agapie T, et al. (2009) NO formation by a catalytically self-sufficient bacterial nitric oxide synthase from Sorangium cellulosum. *Proc Natl Acad Sci USA* 106(38): 16221–16226.
40. McMillan K, Masters BSS (1995) Prokaryotic expression of the heme- and flavin-binding domains of rat neuronal nitric oxide synthase as distinct polypeptides: Identification of the heme-binding proximal thiolate ligand as cysteine-415. *Biochemistry* 34(11):3686–3693.
41. Fossetta JD, et al. (1996) Expression of human inducible nitric oxide synthase in Escherichia coli. *FEBS Lett* 379(2):135–138.
42. Mitchell DA, Erwin PA, Michel T, Marletta MA (2005) S-Nitrosation and regulation of inducible nitric oxide synthase. *Biochemistry* 44(12):4636–4647.
43. Rusche KM, Spiering MM, Marletta MA (1998) Reactions catalyzed by tetrahydrobiopterin-free nitric oxide synthase. *Biochemistry* 37(44):15503–15512.
44. Weis DD, Engen JR, Kass IJ (2006) Semi-automated data processing of hydrogen exchange mass spectra using HX-Express. *J Am Soc Mass Spectrom* 17(12):1700–1703.
45. Hevel JM, Marletta MA (1994) Nitric-oxide synthase assays. *Methods Enzymol* 233: 250–258.
46. Huang P-S, et al. (2011) RosettaRemodel: A generalized framework for flexible backbone protein design. *PLoS ONE* 6(8):e24109.
47. Gray JJ, et al. (2003) Protein-protein docking with simultaneous optimization of rigid-body displacement and side-chain conformations. *J Mol Biol* 331(1):281–299.
48. Kulp DW, et al. (2012) Structural informatics, modeling, and design with an open-source Molecular Software Library (MSL). *J Comput Chem* 33(20):1645–1661.
49. Defays D (1977) An efficient algorithm for a complete link method. *Comput J* 20: 364–366.